Supporting Information for

Synthesis and Modeling of Uniform Complex Metal Oxides by Close-Proximity Atmospheric Pressure Chemical Vapor Deposition

Robert L. Z. Hoye,[†] David Muñoz-Rojas, [†,‡] Kevin P. Musselman,[§,†] Yana Vaynzof,[§,∥] and Judith L. MacManus-Driscoll[,†]*

[†]Department of Materials Science and Metallurgy, University of Cambridge, 27 Charles Babbage Road, Cambridge CB3 0FS, UK

[‡]LMGP, University Grenoble-Alpes, CNRS, F-3800 Grenoble, France

[§]Department of Physics, University of Cambridge, JJ Thomson Avenue, Cambridge CB3 0HE, UK

[∥]Current address: Centre for Advanced Materials, Heidelberg University, Im Neuenheimer Feld 227, Heidelberg, Germany

*E-mail: jld35@cam.ac.uk

Section S1. Time taken for precursor vapors to reach the gas manifold

The pipes downstream of the $Mg(CpEt)_2$ bubbler consist of a 40 cm length of 4 mm internal diameter pipe to the header, followed by a 30 cm length of 1.5 mm internal diameter pipe to the gas manifold (illustrated in Figure 1 of the manuscript). The minimum total gas flow rate in this metal precursor gas line is 125 $mL.min^{-1}$ and maximum gas flow rate is 606.7 $mL.min^{-1}$. Assuming the residence time of the gas in the header is negligible, the maximum time taken is thus calculated in Eq. S1:

$$\text{time} = \text{time(large pipe)} + \text{time(small pipe)} = 60\left(\frac{40\times\frac{\pi}{4}\times 0.4^2}{125} + \frac{30\times\frac{\pi}{4}\times 0.15^2}{125}\right) = 3\,\text{s} \qquad \text{(S1)}$$

The minimum taken is calculated in Eq. S2:

$$\text{time} = \text{time(large pipe)} + \text{time(small pipe)} = 60\left(\frac{40\times\frac{\pi}{4}\times 0.4^2}{606.7} + \frac{30\times\frac{\pi}{4}\times 0.15^2}{606.7}\right) = 0.5\,\text{s} \qquad \text{(S2)}$$

The residence time of the gas in the pipes before reaching the gas manifold is therefore between 0.5 and 3 s.

Section S2. Developing the model and optimizing the growth of AP-CVD $Zn_{1-x}Mg_xO$

The synthesis of $Zn_{1-x}Mg_xO$ is complicated by the Mg precursor (bis(ethylcyclopentyldienyl)magnesium or $Mg(CpEt)_2$) having a much lower vapor pressure than the Zn precursor (diethylzinc or DEZ).[1,2] In order to obtain sufficient Mg incorporation into ZnO, the bubbling rate through the $Mg(CpEt)_2$ should be higher and the Mg precursor heated. We optimized these parameters using the following process:

1. Prediction of the minimum bubbling rate ratio using an idealized model

2. Experimentally optimizing the heating temperature of the Mg precursor

Development of the idealized model

For the optimization process, we first developed an idealized model that had the following assumptions: (i) DEZ and $Mg(CpEt)_2$ have the same reactivities and deposition rates to the substrate, so that the amount of Mg incorporated into the film is the same as the gas fraction of $Mg(CpEt)_2$ ($x = x_{gas}$), (ii) Mg is uniformly distributed in the multicomponent metal oxide produced, (iii) the process is occurring at steady-state, (iv) the gases are ideal, (v) the nitrogen gas flowing from the bubblers is saturated with the precursor, (vi) the carrier gas is pure nitrogen. While the first and fifth assumptions may not be fulfilled, they are difficult to measure and therefore made in our idealized model. We take them to account later in this section.

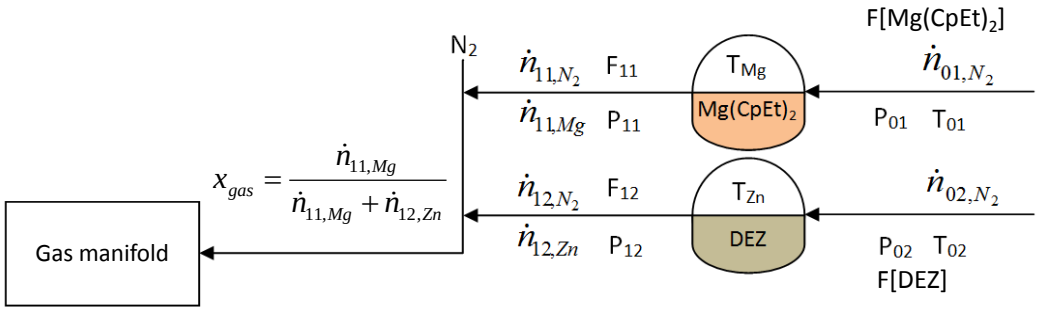

Figure S1. Block flow diagram to illustrate the nomenclature used to develop the model, which are defined immediately below in Table S1. Essentially, N_2 gas is bubbled through the Mg precursor, heated at T_{Mg}. The gas stream from the Mg precursor ($Mg(CpEt)_2$) bubbler has $\dot{n}_{11,Mg}$ of N_2 gas with $Mg(CpEt)_2$ vapor flowing. Similarly, N_2 gas bubbled through the Zn precursor (DEZ, at temperature T_{Zn}) has $\dot{n}_{12,Zn}$ of gas with DEZ vapor flowing. The gas fraction of $Mg(CpEt)_2$ in this gas mixture fed to the gas manifold is thus x_{gas}.

Table S1. Nomenclature for Figure S1.

Symbol	Meaning
x_{gas}	Gas fraction of $Mg(CpEt)_2$ fed to the gas manifold
$F[Mg(CpEt)_2]$	Inlet volumetric flow rate for the $Mg(CpEt)_2$ bubbler
P_{01}	Pressure of inlet line to the $Mg(CpEt)_2$ bubbler
T_{01}	Temperature of inlet line to the $Mg(CpEt)_2$ bubbler
$\dot{n}_{01,N_2}$	Molar flow rate of N_2 in inlet line to $Mg(CpEt)_2$ bubbler
F_{11}	Volumetric flow rate of line from $Mg(CpEt)_2$ bubbler
P_{11}	Pressure of line from $Mg(CpEt)_2$ bubbler
T_{Mg}	Temperature of $Mg(CpEt)_2$ bubbler
$y_{11,Mg}$	Gas fraction of $Mg(CpEt)_2$ in the bubbler
x_{Mg}	Liquid fraction of $Mg(CpEt)_2$ in the bubbler
$\dot{n}_{11,N_2}$	Molar flow rate of N_2 in line from $Mg(CpEt)_2$ bubbler
$\dot{n}_{11,Mg}$	Molar flow rate of Mg from $Mg(CpEt)_2$ bubbler
$F[DEZ]$	Inlet volumetric flow rate to DEZ bubbler
P_{02}	Pressure of inlet line to DEZ bubbler
T_{02}	Temperature of inlet line to DEZ bubbler
$\dot{n}_{02,N_2}$	Molar flow rate of N_2 in inlet line to DEZ bubbler
F_{12}	Volumetric flow rate of line from DEZ bubbler
P_{12}	Pressure of line from DEZ bubbler
T_{Zn}	Temperature of DEZ bubbler
$y_{11,Zn}$	Gas fraction of DEZ in the bubbler
x_{Zn}	Liquid fraction of DEZ in the bubbler
$\dot{n}_{12,N_2}$	Molar flow rate of N_2 in line from DEZ bubbler
$\dot{n}_{12,Zn}$	Molar flow rate of DEZ from DEZ bubbler
p^*_{Mg}	Vapor pressure of $Mg(CpEt)_2$
p^*_{Zn}	Vapor pressure of DEZ

Modeling gas flows through the $Mg(CpEt)_2$ bubbler:

$$\dot{n}_{01,N_2} = \frac{P_{01}F[Mg(CpEt)_2]}{RT_{01}}$$ (ideal gas law on inlet gas) (S3)

$$\dot{n}_{11,N_2} + \dot{n}_{11,Mg} = \dot{n}_{01,N_2}$$ (continuous process => ∑(amount in) =∑(amount out))[3] (S4)

$$P_{11}y_{11,Mg} = p^*_{Mg}(T_{Mg})x_{Mg}$$ (Raoult's Law on $Mg(CpEt)_2$) (S5)

$$y_{11,Mg} = \frac{p^*_{Mg}(T_{Mg})}{P_{11}}$$ (x_{Mg} = 1, assuming no precursor contamination or dilution) (S6)

$$\dot{n}_{11,Mg} = (\dot{n}_{11,Mg} + \dot{n}_{11,N_2})y_{11,Mg}$$ (S7)

$$\dot{n}_{11,Mg} = \dot{n}_{01,N_2}.y_{11,Mg}$$ (S8)

$$\dot{n}_{11,Mg} = \frac{P_{01}F[Mg(CpEt)_2)]}{RT_{01}}\frac{p^*_{Mg}(T_{Mg})}{P_{11}}$$ (S9)

Modeling gas flows through the DEZ bubbler:

$$\dot{n}_{02,N_2} = \frac{P_{02}F[DEZ]}{RT_{02}}$$ (ideal gas law on inlet gas) (S10)

$$\dot{n}_{12,N_2} + \dot{n}_{12,Zn} = \dot{n}_{02,N_2}$$ (continuous process => ∑(amount in) =∑(amount out))[3] (S11)

$$P_{12}y_{12,Zn} = p^*_{Zn}(T_{Zn})x_{Zn}$$ (Raoult's Law on DEZ) (S12)

$$y_{11,Zn} = \frac{p^*_{Zn}(T_{Zn})}{P_{12}}$$ (x_{Zn} = 1, assuming no precursor contamination or dilution) (S13)

$$\dot{n}_{12,Zn} = (\dot{n}_{12,Zn} + \dot{n}_{12,N_2})y_{12,Zn}$$ (S14)

$$\dot{n}_{12,Zn} = \dot{n}_{02,N_2}.y_{12,Zn}$$ (S15)

$$\dot{n}_{12,Zn} = \frac{P_{02}F[DEZ]}{RT_{02}}.\frac{p^*_{Zn}(T_{Zn})}{P_{12}}$$ (S16)

From the block flow diagram of our deposition system shown in Figure S1, Eq. S17 can be expressed, with the nomenclature form shown in Eq. S18.

$$(\text{gas fraction of } \mathrm{Mg(CpEt)_2}) = \frac{\text{molar flow rate of } \mathrm{Mg(CpEt)_2}}{\text{molar flow rate of } \mathrm{Mg(CpEt)_2} + \text{molar flow rate of DEZ}} \quad \text{(S17)}$$

$$x_{gas} = \frac{\dot{n}_{11,Mg}}{\dot{n}_{11,Mg} + \dot{n}_{12,Zn}} = \frac{\dfrac{P_{01}F[Mg(CpEt)_2]}{RT_{01}}\dfrac{p^*_{Mg}(T_{Mg})}{P_{11}}}{\dfrac{P_{01}F[Mg(CpEt)_2]}{RT_{01}}\dfrac{p^*_{Mg}(T_{Mg})}{P_{11}} + \dfrac{P_{02}F[DEZ]}{RT_{02}}.\dfrac{p^*_{Zn}(T_{Zn})}{P_{12}}} \quad \text{(S18)}$$

In Eq. S18 we use $\dot{n}_{11,Mg}$ for the molar flow rate of $Mg(CpEt)_2$ vapor fed to the gas manifold and $\dot{n}_{12,Zn}$ for the molar flow rate of DEZ vapor fed to the gas manifold. P_{01} is the pressure and T_{01} the temperature of the inlet N_2 to the $Mg(CpEt)_2$ bubbler, while P_{11} is the pressure of the gas outlet from that bubbler. P_{02} is the pressure and T_{02} the temperature of the inlet N_2 to the DEZ bubbler, while P_{12} is the pressure of the gas outlet from the DEZ bubbler. Eq. S18 also uses $p^*_{Zn}(T_{Zn})$ for the vapor pressure of DEZ at temperature T_{Zn}, and $p^*_{Mg}(T_{Mg})$ for the vapor pressure of $Mg(CpEt)_2$ at temperature T_{Mg}.

To simplify Eq. S18, it was also assumed that the pressure of the gas streams were the same going in to the metal precursor bubblers (i.e., $P_{01} = P_{02}$), and also coming out from them (i.e., $P_{11} = P_{12}$), as well as these two streams being at the same temperature ($T_{01} = T_{02}$). By applying these assumptions, Eq. S18 can be simplified to Eq. S19 (our idealized model):

$$x_{gas} = \frac{F[Mg(CpEt)_2].p^*_{Mg}(T_{Mg})}{F[Mg(CpEt)_2].p^*_{Mg}(T_{Mg}) + F[DEZ].p^*_{Zn}(T_{Zn})} = \frac{1}{1 + \dfrac{F[DEZ]}{F[Mg(CpEt)_2]}.\dfrac{p^*_{Zn}(T_{Zn})}{p^*_{Mg}(T_{Mg})}} \quad \text{(S19)}$$

Using the idealized model to predict the minimum bubbling rate ratio

To use this idealized model, the vapor pressures of the precursors are needed. DEZ was maintained at room temperature and we used the vapor pressure quoted by our supplier (12.2 mmHg from Sigma-Aldrich).[2] The vapor pressure curve of $Mg(CpEt)_2$ is not reported, with very few reports of its vapor pressure at certain temperatures. It was therefore necessary to interpolate between published values.

Bis(ethylcyclopentadienyl)magnesium (or $Mg(CpEt)_2$) has a vapor pressure of 0.045 mmHg at room temperature and 0.12 mmHg at 65 °C.[1,4] These were two of the very few vapor pressures of $Mg(CpEt)_2$ available in the literature. Fitting a linear Antoine expression to these data points gives the following:

$$p^*_{Mg}(T_{Mg}) = 10^{-\frac{1150}{T}} + 2.5 \qquad \text{(S20)}$$

This approximation is valid since the heating temperatures of $Mg(CpEt)_2$ explored are within the 25 °C – 65 °C range; i.e., interpolation, rather than extrapolation is employed.

According to the fitted curve, the vapor pressure of the $Mg(CpEt)_2$ was 0.08 mmHg at 50 °C, 0.09 mmHg at 55 °C, 0.11 mmHg at 60 °C and 0.12 mmHg at 65 °C. These four heating temperatures of $Mg(CpEt)_2$ were investigated because it was found that the minimum heating temperature to obtain a MgO film was 50 °C, whereas heating to 80 °C led to rapid precusor depletion. The Mg contents for the different heating temperatures as a function of the precursor bubbling rate ratio are calculated using Eq. S19 and shown in Figure S2. This showed that the bubbling rate through the Mg precursor should be at least 25 times more than through the Zn precursor to obtain $x > 0.1$. To achieve this, the bubbling rate through the Mg precursor should be >100 $mL.min^{-1}$ and <10 $mL.min^{-1}$ through the Zn precursor. This can be

obtained using a flowmeter with the range of 100 – 500 mL.min^{-1} for the Mg precursor, and a flowmeter with the range of 0 – 10 mL.min^{-1} for the Zn precursor, rather than the flowmeters with a range of 10 – 100 mL.min^{-1}, which are normally used for the deposition of simple binary metal oxides (e.g., ZnO and TiO_2).[5,6] After predicting the minimum bubbling rate ratio of 25:1 (F[$Mg(CpEt)_2$:F[DEZ]) using our idealized model, the deposition temperature was experimentally opitmized.

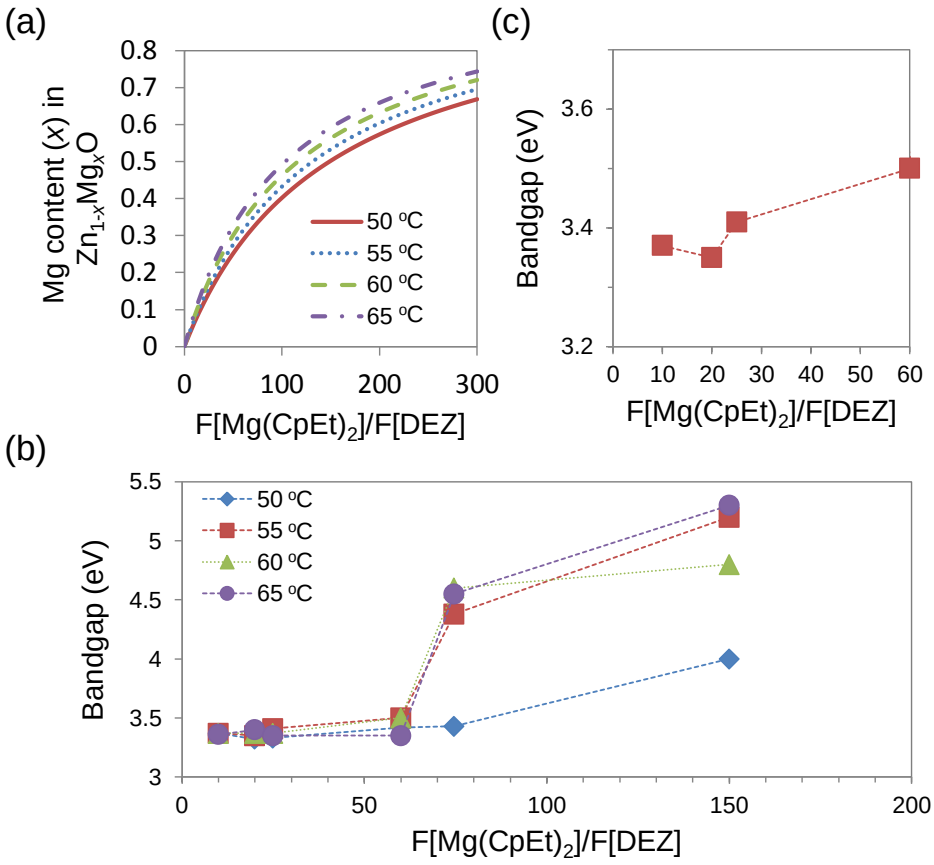

Figure S2. (a) Plot of the calculated Mg content (x) in $Zn_{1-x}Mg_xO$ at different temperatures of the $Mg(CpEt)_2$. F[$Mg(CpEt)_2$] is the N_2 bubbling rate through the Mg precursor and F[DEZ] is the N_2 bubbling rate through the Zn precursor. (b) Measured bandgap vs. different ratios of bubbling through the Mg precursor relative to the Zn precursor. 300 oscillations of the film under the gas manifold were used in all cases. (c) Close-up of the bandgap vs. bubbling rate ratio plot for $Mg(CpEt)_2$ heated to 55 °C, showing that the bandgap does not significantly increase until the bubbling rate ratio is more than 25.

According to previous reports of $Zn_{1-x}Mg_xO$ fabricated using sol-gel,[7] sputtering,[8] and metal-organic chemical vapor deposition,[9] the bandgap is strongly dependent on the Mg content, since the Mg 3s orbital hybridizes with the Zn 4s orbital to control the conduction band minimum position.[10] In our previous work, we showed that the bandgap variation with Mg content has two regions, with a transition between them.[11] However, with increasing Mg content (x), the bandgap increased with small error bars, indicating that adjusting the Mg content finely tunes the bandgap.[11] Conversely, a larger bandgap is a reliable indication of a higher Mg content. We therefore used bandgap measurements of the films as a simple indication of the effect of bubbling rate ratio and $Mg(CpEt)_2$ vapor pressure on the amount of Mg incorporation. Figure S2b shows that heating the Mg precursor above 55 °C led to no significant increase in the bandgap. This would primarily be due to the pipes downstream of the Mg precursor bubbler not being heated (details of the deposition system in Figure 1 of the manuscript). Some of the Mg precursor could therefore have condensed on the inside of the pipelines. However, it takes between 0.5 s and 3 s for the gas mixture to reach the gas manifold (calculated in Section S1). Very little of the total amount of Mg precursor would deposit onto the pipe walls per deposition, since the gas stream is moving very quickly. We also observe that it takes several hours of flowing the Mg precursor through the pipe before a deposit appears on the pipe walls. Nevertheless, the cooling of the gas streams could make 5 °C intervals in Mg precursor heating temperature above 55 °C insignificant. But since it is desirable to minimize precursor depletion by minimizing the heating temperature, and since heating to 55 °C led to larger bandgaps than heating to 50 °C (Figure S2b), 55 °C was selected as the optimum $Mg(CpEt)_2$ heating temperature. From Figure S2c, it can be seen that the bubbling rate ratio did need to be more than 25 in order for the bandgap to be appreciably larger than 3.35 eV when the $Mg(CpEt)_2$ heating temperature was 55 °C, which

is in agreement with the idealized model. The bubbling rates we used are shown in Table 1 of the manuscript.

Refining the model to take into account the different reactivities of the metal precursors:

In the idealized model, it was assumed that the gas fraction of the Mg precursor (x_{gas}) equated to its fraction in the film (x), that is $x_{gas} = x$. We also assumed complete saturation of the precursors in the gas stream exiting from the bubblers. If the deposition reactions of the metal precursors onto the substrate and saturation of each precursor are known, then Eq. S19 can be modified accordingly. For example, if the deposition reaction for each organometallic precursor is independent of each other, first order, and the only reactant is the precursor then Eq. S19 can be modified to give the Mg content in the film (x).

$$x = \frac{k_{Mg}\dot{n}_{11,Mg}}{k_{Mg}\dot{n}_{11,Mg} + k_{Zn}\dot{n}_{12,Zn}} = \frac{k_{Mg}s_{Mg}\dfrac{P_{01}F[Mg(CpEt)_2]}{RT_{01}}\dfrac{p^{*}{}_{Mg}(T_{Mg})}{P_{11}}}{k_{Mg}s_{Mg}\dfrac{P_{01}F[Mg(CpEt)_2]}{RT_{01}}\dfrac{p^{*}{}_{Mg}(T_{Mg})}{P_{11}} + k_{Zn}s_{Zn}\dfrac{P_{02}F[DEZ]}{RT_{02}}.\dfrac{p^{*}{}_{Zn}(T_{Zn})}{P_{12}}} \tag{S21}$$

In Eq. S21, we introduce the new terms s_{Mg} and s_{Zn} to give the fraction by which the Mg and Zn precursors respectively are saturated in their N_2 carrier gas (1 for 100% saturated and 0 for 0% saturated). Eq. S21 can be simplified to Eq. S23 if the same assumptions listed for Eq. S18 are applied:

$$x = \frac{k_{Mg}s_{Mg}F[Mg(CpEt)_2].p^{*}{}_{Mg}(T_{Mg})}{k_{Mg}s_{Mg}F[Mg(CpEt)_2].p^{*}{}_{Mg}(T_{Mg}) + k_{Zn}s_{Zn}F[DEZ].p^{*}{}_{Zn}(T_{Zn})} \tag{S22}$$

$$x = \frac{1}{1 + \dfrac{s_{Zn}}{s_{Mg}}\dfrac{k_{Zn}}{k_{Mg}}\dfrac{F[DEZ]}{F[Mg(CpEt)_2]}.\dfrac{p^{*}{}_{Zn}(T_{Zn})}{p^{*}{}_{Mg}(T_{Mg})}} \tag{S23}$$

In Eq. S23, k_{Mg} is the incorporation rate of $Mg(CpEt)_2$ and k_{Zn} is the incorporation rate of DEZ to the film. More complex treatments of different reactivities can be found in an analogous work on ALD reactions.[12]

Section S3. Growth rates of $Zn_{1-x}Mg_xO$

The growth rate per cycle of the films can be determined from a plot of thickness against the number of deposition cycles.[13] The thicknesses were measured by Dektak profilometry according to a previously reported method.[5] Each cycle took 1 s, meaning that the growth rate per cycle and temporal growth rate have the same numerical value. In Table 1 in the manuscript, the temporal growth rates are shown, since this is more appropriate for films deposited by AP-CVD.

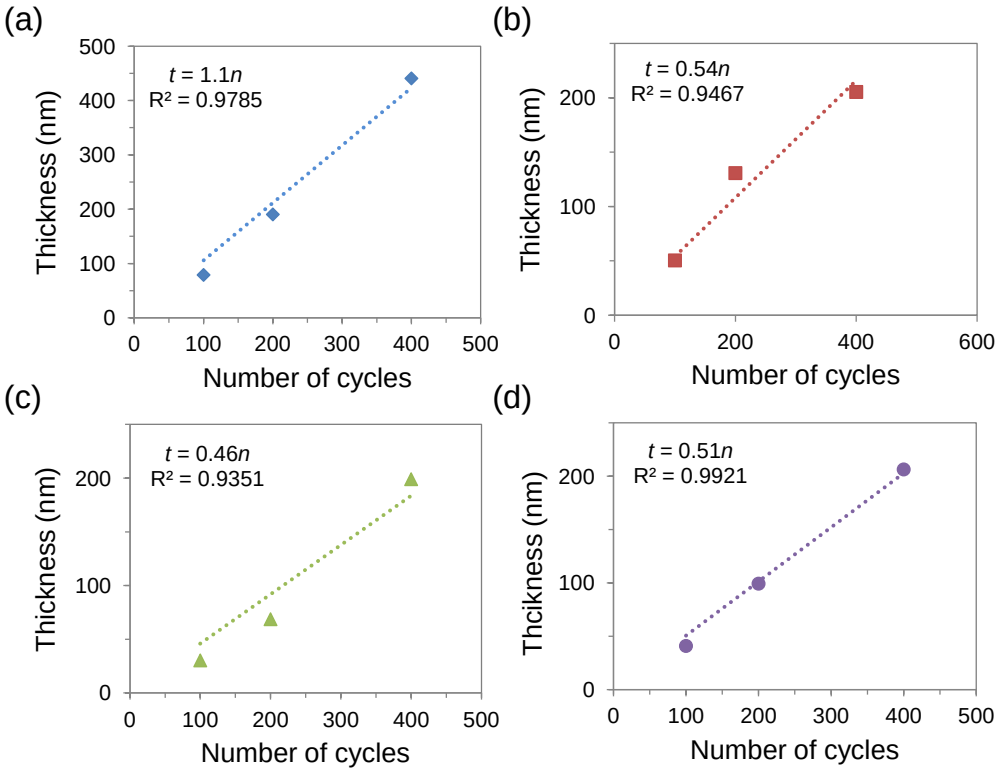

Figure S3. Plot of the average film thickness vs. number of cycles to determine the growth rate of (a) ZnO, (b) $Zn_{0.8}Mg_{0.2}O$, (c) $Zn_{0.58}Mg_{0.42}O$ and (d) $Zn_{0.4}Mg_{0.6}O$. The compositions we show are taken to be the same as those of the films specifically measured by XPS.

Section S4. $Zn_{1-x}Mg_xO$ film properties

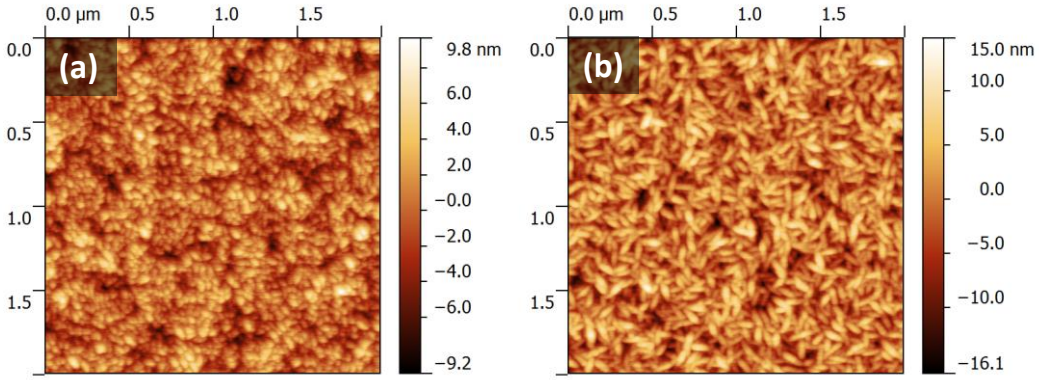

Figure S4. AFM measurements of (a) ZnO and (b) $Zn_{0.54}Mg_{0.46}O$ on ITO/glass showing that the films are crystalline when deposited at 150 °C. We also note that the morphology of our AP-CVD ZnO films is very similar to that of ALD ZnO (given in ref 14).

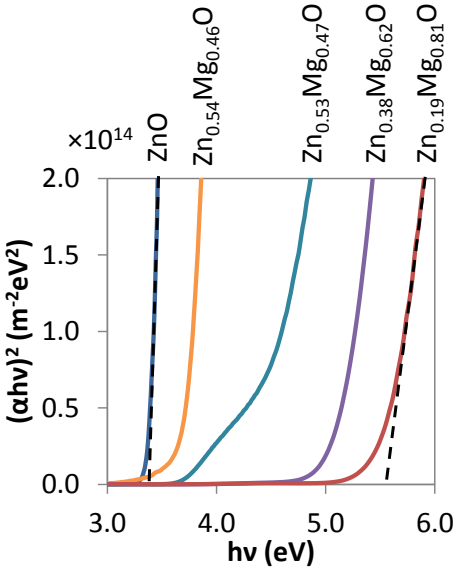

Figure S5. Tauc plots of $Zn_{1-x}Mg_xO$ films over a doping range, showing that the bandgap increased from 3.3 eV (x = 0) to 5.5 eV (x = 0.81).

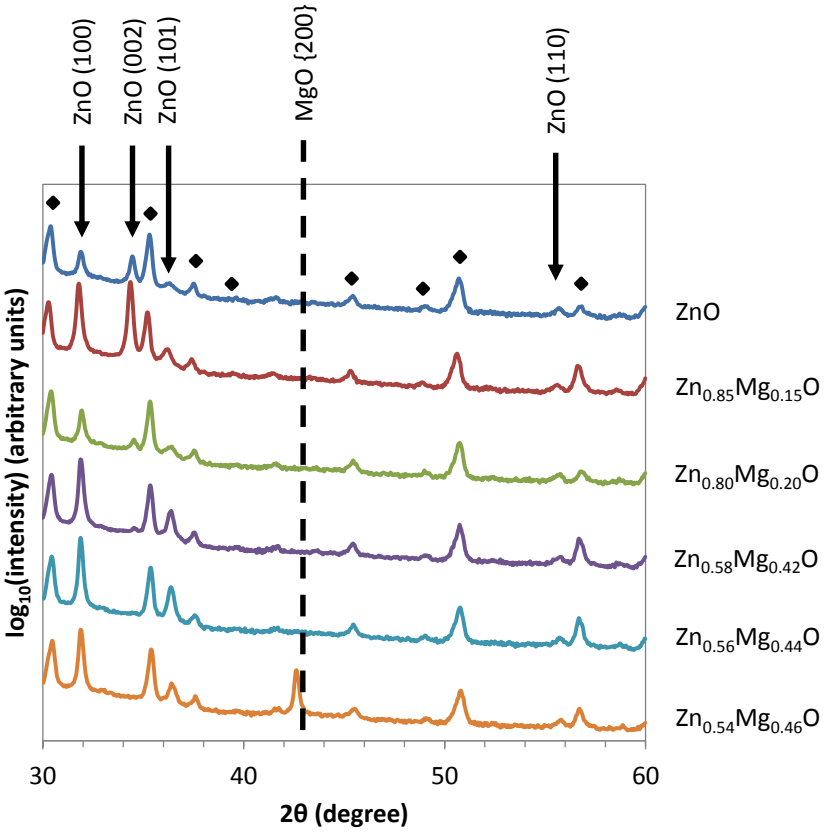

Figure S6. X-ray diffraction patterns of $Zn_{1-x}Mg_xO$ on ITO/glass (same as in Figure 5 of the manuscript) post-annealed at 400 °C for 1 h in air.

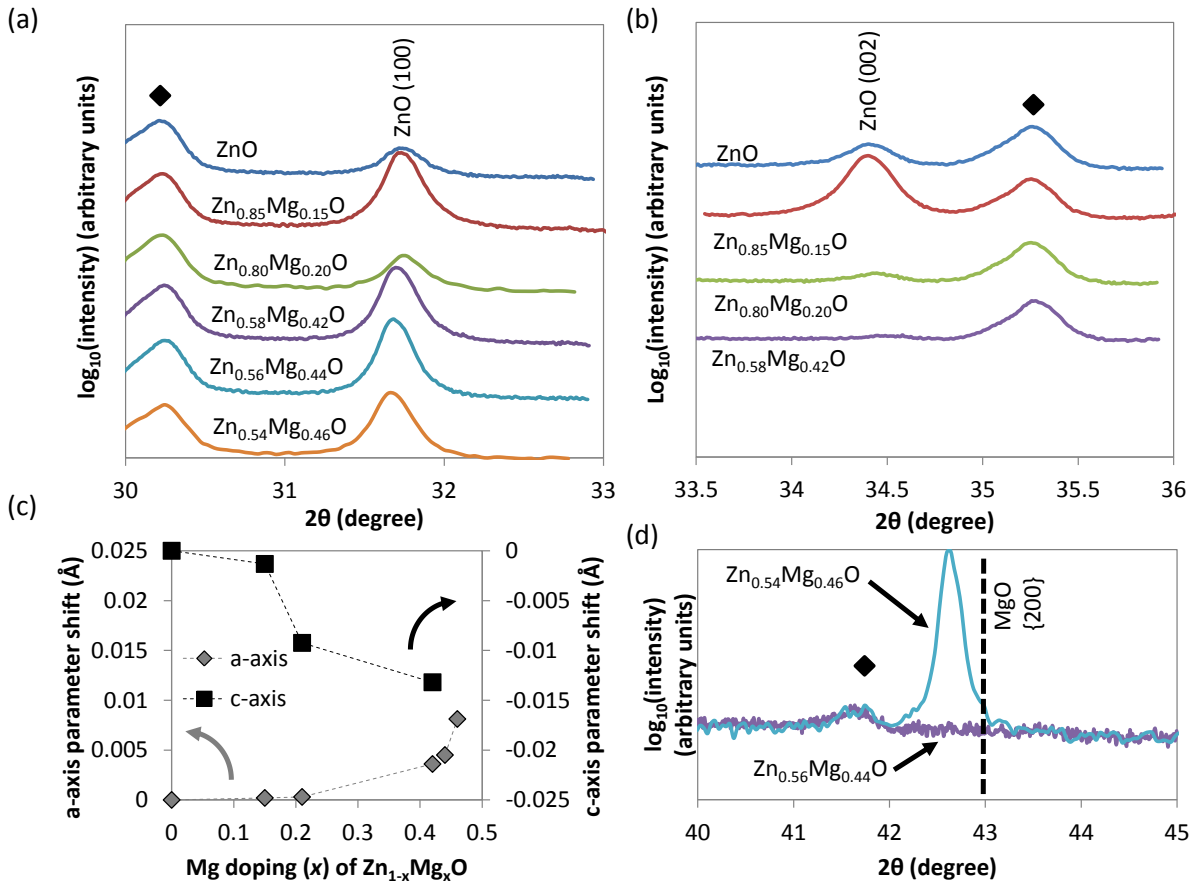

Figure S7. X-ray diffraction patterns of $Zn_{1-x}Mg_xO$ post-annealed at 400 °C for 1 h in air. (a) Scans of the wurtzite (100) and (b) wurtzite (002) peaks. (c) Change in the c-axis and a-axis parameters with Mg incorporation. (d) Comparison of the diffraction patterns of post-annealed $Zn_{0.56}Mg_{0.44}O$ and $Zn_{0.54}Mg_{0.46}O$ showing that $Zn_{0.56}Mg_{0.44}O$ did not have any detectable second phase after post-annealing.

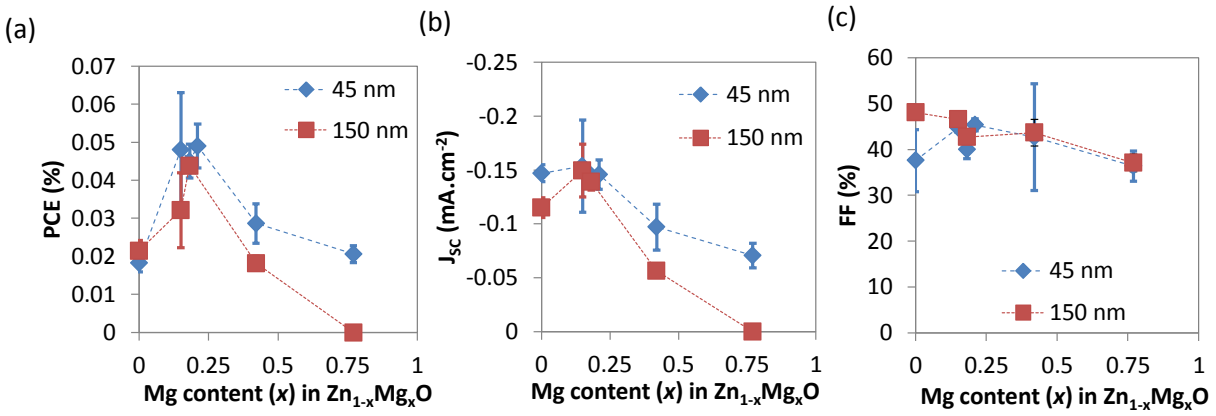

Figure S8. (a) Efficiency (*PCE*), (b) short-circuit current density (J_{SC}) and (c) fill factor (*FF*) of hybrid poly(3-hexylthiophene-2,5-diyl) (P3HT) devices with 45 nm and 150 nm thick $Zn_{1-x}Mg_xO$ at different Mg incorporation (x) levels.

References

(1) Bis(ethylcyclopentadienyl)magnesium; Strem Chemicals, Inc. URL: http://www.strem.com/catalog/msds/98-4006.

(2) Diethylzinc; SAFC Hitech. URL: http://www.sigmaaldrich.com/content/dam/sigma-aldrich/docs/Sigma-Aldrich/General_Information/epichem-zinc.pdf.

(3) Felder, R. M.; Rousseau, R. W. *Elementary Principles of Chemical Processes*, 3rd ed.; John Wiley & Sons, Inc: New York, USA, 2005.

(4) Nakamura, A.; Yamamoto, K.; Ishihara, J.; Aoki, T.; Temmyo, J. Characterization of $Mg_xZn_{1-x}O$ Films Grown by Remote-Plasma-Enhanced Metalorganic Chemical Vapor-Deposition Using Bis-Ethylcyclopentadienyl Magnesium. *Jpn. J. Appl. Phys.* **2005**, *44*, 7267–7270.

(5) Hoye, R. L. Z.; Muñoz-Rojas, D.; Iza, D. C.; Musselman, K. P.; MacManus-Driscoll, J. L. High Performance Inverted Bulk Heterojunction Solar Cells by Incorporation of Dense, Thin ZnO Layer Made Using Atmospheric Atomic Layer Deposition. *Sol. Energy Mater. Sol. Cells* **2013**, *116*, 197–202.

(6) Muñoz-Rojas, D.; Sun, H.; Iza, D. C.; Weickert, J.; Chen, L.; Wang, H.; Schmidt-Mende, L.; MacManus-Driscoll, J. L. High-Speed Atmospheric Atomic Layer Deposition of Ultra Thin Amorphous TiO_2 Blocking Layers at 100 °C for Inverted Bulk Heterojunction Solar Cells. *Prog. Photovoltaics* **2013**, *21*, 393–400.

(7) Olson, D. C.; Shaheen, S. E.; White, M. S.; Mitchell, W. J.; van Hest, M. F. A. M.; Collins, R. T.; Ginley, D. S. Band-Offset Engineering for Enhanced Open-Circuit Voltage in Polymer–Oxide Hybrid Solar Cells. *Adv. Funct. Mater.* **2007**, *17*, 264–269.

(8) Thapa, D.; Huso, J.; Che, H.; Huso, M.; Morrison, J. L.; Gutierrez, D.; Grant Norton, M.; Bergman, L. Probing Embedded Structural Inhomogeneities in MgZnO Alloys via Selective Resonant Raman Scattering. *Appl. Phys. Lett.* **2013**, *102*, 191902.

(9) Duan, Z.; Du Pasquier, A.; Lu, Y.; Xu, Y.; Garfunkel, E. Effects of Mg Composition on Open Circuit Voltage of Cu_2O–$Mg_xZn_{1-x}O$ Heterojunction Solar Cells. *Sol. Energy Mater. Sol. Cells* **2012**, *96*, 292–297.

(10) Bai, L.-N.; Lian, J.-S.; Jiang, Q. Optical and Electronic Properties of Wurtzite Structure $Zn_{1-x}Mg_xO$ Alloys. *Chin. Phys. Lett.* **2011**, *28*, 117101.

(11) Hoye, R. L. Z.; Ehrler, B.; Böhm, M. L.; Muñoz-Rojas, D.; Altamimi, R. M.; Alyamani, A. Y.; Vaynzof, Y.; Sadhanala, A.; Ercolano, G.; Greenham, N. C.; Friend, R. H.; MacManus-Driscoll, J. L.; Musselman, K. P. Improved Open-Circuit Voltage in ZnO-PbSe Quantum Dot Solar Cells by Understanding and Reducing Losses Arising from the ZnO Conduction Band Tail. *Adv. Energy Mater.* **2014**, *4*, 1301544.

(12) Holmqvist, A.; Törndahl, T.; Stenström, S. A Model-Based Methodology for the Analysis and Design of Atomic Layer Deposition processes—Part III: Constrained Multi-Objective Optimization. *Chem. Eng. Sci.* **2013**, *96*, 71–86.

(13) Torndahl, T.; Platzer-Bjorkman, C.; Kessler, J.; Edoff, M. Atomic Layer Deposition of $Zn_{1-x}Mg_xO$ Buffer Layers for $Cu(In,Ga)Se_2$ Solar Cells. *Prog. Photovoltaics* **2007**, *15*, 225–235.

(14) Tapily, K.; Gu, D.; Baumgart, H.; Namkoong, G.; Stegall, D.; Elmustafa, A. A. Mechanical and Structural Characterization of Atomic Layer Deposition-Based ZnO Films. *Semicond. Sci. Technol.* **2011**, *26*, 115005.